Published in final edited form as:
Phys Chem Chem Phys. 2010 December 7; 12(45): 14873–14883. doi:10.1039/c0cp00795a.

Determination of Relative Tensor Orientations by γ-encoded Chemical Shift Anisotropy/Heteronuclear Dipolar Coupling 3D NMR Spectroscopy in Biological Solids

Guangjin Hou[a,b], **Sivakumar Paramasivam**[a], **In-Ja L. Byeon**[b,c], **Angela M. Gronenborn**[b,c], and **Tatyana Polenova**[a,b]

[a]Department of Chemistry and Biochemistry, University of Delaware, Newark, Delaware 19716, United States

[b]Pittsburgh Center for HIV Protein Interactions, University of Pittsburgh School of Medicine, 1051 Biomedical Science Tower 3, 3501 Fifth Ave., Pittsburgh, PA 15261, United States

[c]Department of Structural Biology, University of Pittsburgh School of Medicine, 1051 Biomedical Science Tower 3, 3501 Fifth Ave., Pittsburgh, PA 15261, United States

Abstract

In this paper, we present 3D chemical shift anisotropy (CSA)/dipolar coupling correlation experiments, based on γ-encoded R-type symmetry sequences. The γ-encoded correlation spectra are exquisitely sensitive to the relative orientation of the CSA and dipolar tensors and can provide important structural and dynamic information in peptides and proteins. We show that the first-order ($m = \pm 1$) and second-order ($m = \pm 2$) Hamiltonians in the R-symmetry recoupling sequences give rise to different correlation patterns due to their different dependencies on the crystallite orientation. The relative orientation between CSA and dipolar tensors can be determined by fitting the corresponding correlation patterns. The orientation of ^{15}N CSA tensor in the quasi-molecular frame is determined by the relative Euler angles, α_{NH} and β_{NH}, when the combined symmetry schemes are applied for orientational studies of ^{1}H-^{15}N dipolar and ^{15}N CSA tensors. The correlation experiments introduced here work at moderate magic angle spinning frequencies (10-20 kHz) and allow for simultaneous measurement of multiple sites of interest. We studied the orientational sensitivity of γ-encoded symmetry-based recoupling techniques numerically and experimentally. The results are demonstrated on [^{15}N]-*N*-acetyl-valine (NAV) and *N*-formyl-Met-Leu-Phe (MLF) tripeptide.

Introduction

Three-dimensional structures of peptides, proteins and protein assemblies at atomic-level resolution provide important clues for understanding their biological function. Solid-state nuclear magnetic resonance (SSNMR) is emerging as an important technique for structural elucidation of biological systems,[1] and is particularly powerful for studies of large biopolymers, such as membrane proteins,[2-8] amyloid fibrils,[9-12] intact viruses,[13, 14] and protein assemblies.[15, 16] Even for globular, soluble proteins, SSNMR is becoming an essential structural tool since solid-state NMR observables inform about properties of the

---

Correspondence to: Tatyana Polenova.

Supporting Information: The recoupled lineshapes for different crystallite orientations in the laboratory frame produced by γ-encoded $R18_1^7$ and $R14_2^{3/5}$. The effect of the Euler angle α_{NH} on the 2D DIP/CSA lineshapes for the simulated DIP/CSA correlation spectra acquired with the γ-encoded $R18_1^7$ and $R14_2^{3/5}$ pulse sequences. Simulated $R18_1^7/R14_2^5$ DIP/CSA correlation spectra for different relative tensor orientations.

system at hand that are unavailable from solution measurements.[17-26] For example, the anisotropic spin interactions, such as chemical shift (CS) and dipolar interactions, bear a wealth of information about the geometric and electronic structure of a wide variety of solid systems including organic polymers and proteins.[18, 25-34] In MAS experiments, these anisotropic spin interactions are averaged out partially or completely by the rapid spinning of the sample around the fixed axis at "magic angle". In order to measure and exploit these anisotropic interactions, SSNMR recoupling methods have been developed that restore the geometric and electronic structure information.[35-49] Alternatively, anisotropic interactions can also be measured under static conditions; however, site resolution is limited in the solid powders, and for multiple sites in a system, it is advantageous to carry out such measurements on aligned samples.[50-54]

Among the numerous recoupling techniques,[35-44, 55] one class of methods, developed by M. Levitt,[56-59] employs a symmetry-based principle for the design of pulse sequences that are based on the use of rotor-synchronized radio-frequency (rf) fields in conjunction with magic angle spinning. There are two main symmetry-based pulse sequence classes, CN_n^{ν} and RN_n^{ν}, where the symbols N, n and ν are small integers and are referred to as the symmetry numbers of the pulse sequence. The CN_n^{ν} sequences are designed such, that no net rotation of the spin angular momenta is produced as the result of the rotor-synchronized train of radiofrequency pulses, the so-called the C blocks. In the RN_n^{ν} sequences, a net rotation of the spin angular momenta by π around the x axis of the rotating frame is created. Comparing these two classes of symmetry-based sequences, the R-type sequences have more restrictive selection rules than the C-type sequences.[40, 59, 60] The choice of any particular symmetry-based recoupling sequence depends on the tensorial interaction of interest and on the experimental conditions (i.e., the range of MAS frequencies and rf fields) available to the NMR spectroscopist.

Knowledge about the magnitude and orientation of the ^{15}N chemical shift anisotropy (CSA) tensor is important for biological solids because it provides critical information on the primary/secondary structure, electrostatics, hydrogen bonding, solvation, and dynamics.[54, 61, 62] Although the magnitudes of the three principal elements of the ^{15}N CSA tensor can be measured easily with existing methods in non-single-crystalline solids under MAS conditions, these experiments do not provide any direct information about the orientation of the CSA tensor in the molecular frame. In contrast, for single crystalline solids, both the magnitude and orientation of the three principal elements of the CSA tensor can be determined by the NMR measurement.[62] However, many interesting biological systems (e.g., membrane proteins, protein assemblies, and other biopolymers) cannot be prepared as single crystals, and therefore development of methods for determination of the orientation of the CSA tensor in such noncrystalline samples under MAS conditions (where the resolution and the sensitivity of the measurements is the highest) is becoming more and more important.

For orienting the ^{15}N CSA tensor in the molecular frame, the three Euler angles (α, β, γ) are required, but there is no SSNMR approach for determining γ directly. However, since to an excellent approximation, the δ_{zz} principal component of the ^{15}N CSA tensor lies in the peptide plane and the Euler angle γ is usually close to zero, it is reasonable to postulate that the orientation of ^{15}N CSA tensor is determined by α and β in the quasi-molecular frame. Based on two- and three-dimensional experiments for correlating chemical shift and dipolar tensors, several methods have been proposed for characterization of the CSA tensor orientation in the quasi-molecular frame, and these methods have been applied successfully to a number of powder samples.[50, 51, 63-68] PISEMA (Polarization Inversion Spin Exchange at the Magic Angle)[66] and COAST-$C7_2^1$ (Combined offset and anisotropy stabilization)[63] can be used to extract the orientation of the CSA tensor, however these types of experiments are performed under static or slow magic angle spinning conditions, making them suitable for studying only a single site of interest. For a system containing multiple sites, PISEMA or COAST-C7_2^1 suffer from peak overlap, interfering with the simultaneous determination of the relative orientations of ^{15}N CSA tensors in a site-resolved manner.

In this work, we demonstrate a three-dimensional MAS NMR approach based on γ-encoded R-type symmetry sequences, in which dipolar and CSA interactions are re-introduced into the t_1 and t_2 indirect dimensions, respectively. The resulting correlation spectra are especially sensitive to the relative orientation of the CSA and dipolar tensors. The experiments introduced here work at moderate MAS frequencies (10-20 kHz) and yield orientational information simultaneously for multiple sites. The orientational sensitivity of γ-encoded symmetry-based recoupling techniques was studied numerically and experimentally. Results are demonstrated on [^{15}N]-*N*-acetyl-valine (NAV) and *N*-formyl-Met-Leu-Phe (MLF) tripeptide.

Theoretical background: a *γ*-encoded symmetry-based recoupling approach

Consider a system of coupled *S* spins undergoing a mechanical rotation about a fixed axis. The spin Hamiltonian of such system in the presence of an rf pulse irradiation consists of the time-dependent rf Hamiltonian and the time-dependent internal Hamiltonian, and can be expressed as[58, 60]

$$H(t)=H_{rf}(t)+H_{\mathrm{int}}(t) \tag{1}$$

$$H_{\mathrm{int}}(t)=\sum_{\Lambda,l,m,\lambda,\mu} H^{\Lambda}_{lm\lambda\mu}(t) \tag{2}$$

with the quantum numbers l and λ indicating the rank of the spin interaction Λ with respect to spatial rotation and spin rotations, respectively. m ($-l$, $-l+1$, …, $+l$) and μ ($-\lambda$ - $\lambda+1$, …, $+\lambda$) refer to the space and spin rotational component, respectively. The rotation of spins caused by the rf irradiation results in the internal Hamiltonian elements with $\mu \neq 0$. With the Magnus expansion of the effective Hamiltonian in the interaction frame, the first-order average internal Hamiltonian for t = 0~τ is given by

$$\begin{aligned}\overline{H}^{\Lambda} &= \sum_{l,m,\lambda,\mu} \overline{H}^{\Lambda}_{lm\lambda\mu} \\ &= \sum_{l,m,\lambda,\mu} K_{m\lambda\mu} A^{\Lambda}_{lm}(\Omega_{PR}) d^{l}_{m0}(\beta_{RL}) T^{\Lambda}_{\lambda\mu}\end{aligned} \tag{3}$$

The scaling factor due to the rf irradiation is expressed as

$$K_{m\lambda\mu}=\tau^{-1}\int_0^{\tau} dt \cdot e^{im\varpi_r t+i\mu\gamma_{rf}(t)} d^{\lambda}_{\mu 0}[-\beta_{rf}(t)] \tag{4}$$

With the irradiation by the periodic R$N_n{}^{\nu}$ symmetry pulses, the selection rules for the first-order average Hamiltonian satisfy the following equation:

$$\overline{H}^{\Lambda}_{lm\lambda\mu}=0 \text{ if } mn-\mu\nu \neq \frac{N}{2}Z_{\lambda} \tag{4}$$

with Z_λ an integer with the same parity as λ. On the basis of the different rotational properties of the spin interactions, a given type of interaction can be recoupled selectively by designing the appropriate symmetry pulse sequences. Considering a symmetry-allowed spin Hamiltonian characterized by a particular set of quantum numbers {*l*, *m*, *λ*, *μ*}, the component $A^{\Lambda}_{lm}(\Omega_{PR})$ of the spatial tensor in equation (3) has the following form:

$$A^{\Lambda}_{lm}(\Omega_{PR})=\sum_{m''m'}\left[A^{\Lambda}_{lm}\right]^{P} D^{l}_{m''m'}\left(\Omega^{\Lambda}_{PM}\right) D^{l}_{m'm}\left(\Omega_{MR}\right) \tag{6}$$

$$D^{l}_{m'm}\left(\Omega_{MR}\right)=\exp\{-im'\alpha_{MR}\}\, d^{l}_{m'm}\left(\beta_{MR}\right)\exp\{-im\gamma_{MR}\} \tag{7}$$

The magnitude of each single component of the recoupled Hamiltonian is independent of the Euler angle γ_{MR}, and it is only the phase that is γ_{MR}-dependent. *γ*-encoding generally leads to a high recoupling efficiency in a powder and good discrimination of the recoupled spin interactions.[40, 69, 70] In addition, *γ*-encoded recoupling methods are highly sensitive to the molecular orientation, since only the recoupled lineshape and the magnitude depend on two Euler angles, α_{MR} and β_{MR}, which in turn describe the molecular orientation in the rotor frame. Although the complete recoupled spin Hamiltonian usually contains several symmetry-allowed terms which result in a non- *γ*-encoded recoupled Hamitonian, it is possible to design the selection rules for each spatial quantum number associated with a single spin quantum number, thereby maintaining the entire recoupled Hamiltonian *γ*-encoded.

For example, the $R18_1^7$ symmetry sequence suppresses the isotropic chemical shift, heteronuclear *J*-coupling and homonuclear dipolar interactions, but recouples the CSA and heteronuclear dipole-dipole interactions characterized by quantum numbers {*l*, *m*, *λ*, *μ*} = {2, 2, 1,-1} and {2, -2, 1, 1}.[40] Since each spatial component is associated with only a single spin component, the spin Hamitonian recoupled by $R18_1^7$ is *γ*-encoded. Figure 1 represents the selection properties for CSA and heteronuclear dipolar interactions in two other symmetry-based recoupling sequences, $R14_2^3$ and $R14_2^5$. As shown in Figure 1(a), the only Hamiltonian terms that are symmetry-allowed by $R14_2^3$ are {*l*, *m*, *λ*, *μ*} = {2, 2, 1, -1} and {2, -2, 1, 1}. It therefore is a *γ*-encoded recoupling sequence with the same selection rules as $R18_1^7$. The $R14_2^5$ sequence exhibits different selection properties for the spin interactions with *l* = 2 and λ = 1. In $R14_2^5$, the symmetry-allowed terms are {*l*, *m*, *λ*, *μ*} = {2, 1, 1, -1} and {2, -1, 1, 1}, and this sequence is also *γ*-encoded for recoupling of the CSA or heteronuclear dipolar interactions. At the same time, the spin Hamiltonian terms with quantum numbers {*l*, *m*, *λ*, *μ*} = {2, 2, 2, -2} and {2, -2, 2, 2} are also symmetry-allowed in $R14_2^5$, indicating that it too is *γ*-encoded for recoupling the homonuclear dipolar interaction. $R14_2^5$ therefore is a powerful sequence for the determination of heteronuclear dipolar or CSA interactions in systems with weak homonuclear dipolar interactions. In addition, $R14_2^5$ provides higher scaling factors than $R14_2^3$ and $R18_1^7$.

It is important to note that for the recoupling of the CSA interactions, the space-spin selections dictate which terms in the Hamiltonian will be recovered, and these selection rules are different for each specific symmetry-based sequence. The average CSA

Hamiltonian in Equation (3) can be separated into three components, corresponding to the zeroth-order ($m = 0$), the first-order ($m = \pm1$) and the second-order ($m = \pm2$) terms according to the spatial rank number, respectively:[69]

$$\overline{H}_{(0)}^{CSA} = \sum_{m=0,\lambda,\mu} K_{m\lambda\mu} A_{lm}^{\Lambda}(\Omega_{PR}) d_{m0}^{l}(\beta_{RL}) T_{\lambda\mu}^{\Lambda} = \gamma B_0 \sigma_0 I_z \tag{8}$$

$$\overline{H}_{(1)}^{CSA} = \sum_{m=\pm1,\lambda,\mu} K_{m\lambda\mu} A_{lm}^{\Lambda}(\Omega_{PR}) d_{m0}^{l}(\beta_{RL}) T_{\lambda\mu}^{\Lambda} = \gamma B_0 \sigma_1 \cos(\gamma_{PR} + \omega_r t + \delta_1) I_z \tag{9}$$

$$\overline{H}_{(2)}^{CSA} = \sum_{m=\pm2,\lambda,\mu} K_{m\lambda\mu} A_{lm}^{\Lambda}(\Omega_{PR}) d_{m0}^{l}(\beta_{RL}) T_{\lambda\mu}^{\Lambda} = \gamma B_0 \sigma_2 \cos2(\gamma_{PR} + \omega_r t + \delta_2) I_z \tag{10}$$

Here the expressions for σ_0, σ_1, and σ_2 depend on the crystallite orientation and the three principal values of the CSA tensor. It can be seen that the first-order and the second-order CSA Hamiltonian terms can be removed by sample spinning at the magic angle, and a sharp line is observed at σ_0. However, rotor-synchronized pulse irradiation of correct symmetry would selectively recover the CSA Hamiltonian terms. According to the quantum numbers of the symmetry-allowed Hamiltonian terms, $R14_2^5$ and $R14_2^3$ can be referred to as the first-order σ_1 and the second-order σ_2 γ-encoded symmetry sequences, respectively. In this nomenclature, σ_0, σ_1, and σ_2 are expressed as

$$\sigma_0 = \sigma^{iso} + P_2(\cos\beta_{RL})[P_2(\cos\beta_{PR})(\sigma_{zz}^{PAS} - \sigma^{iso}) + \tfrac{1}{2}\sin\beta_{PR}\cos2\alpha_{PR}(\sigma_{xx}^{PAS} - \sigma_{yy}^{PAS})] \tag{11}$$

$$\begin{aligned} \sigma_1 &= \sqrt{\sigma_{COS1}^2 + \sigma_{SIN1}^2} \\ &= \sin\beta_{RL}\cos\beta_{RL}\sin\beta_{PR}[\{\cos\beta_{PR}[-3(\sigma_{zz}^{PAS} - \sigma^{iso}) + \cos2\alpha_{PR}(\sigma_{xx}^{PAS} - \sigma_{yy}^{PAS})]\}^2 + [\sin2\alpha_{PR}(\sigma_{xx}^{PAS} - \sigma_{yy}^{PAS})]^2]^{1/2} \end{aligned} \tag{12}$$

$$\begin{aligned} \sigma_2 &= \sqrt{\sigma_{COS2}^2 + \sigma_{SIN2}^2} \\ &= \tfrac{1}{2}\sin^2\beta_{RL}\{[\tfrac{3}{2}\sin^2\beta_{PR}(\sigma_{zz}^{PAS} - \sigma^{iso}) + \tfrac{1}{2}(1 + \cos2\beta_{PR}) \times \cos2\alpha_{PR}(\sigma_{xx}^{PAS} - \sigma_{yy}^{PAS})]^2 + [\cos\beta_{PR}\sin2\alpha_{PR}(\sigma_{xx}^{PAS} - \sigma_{yy}^{PAS})]^2\}^{1/2} \end{aligned} \tag{13}$$

$$\begin{aligned} \delta_1 &= \tan^{-1}\left(\frac{\sigma_{SIN1}}{\sigma_{COS1}}\right) \\ &= \tan^{-1}\left[\frac{\sin2\alpha_{PR}(\sigma_{xx}^{PAS} - \sigma_{yy}^{PAS})}{\cos\beta_{PR}[-3(\sigma_{zz}^{PAS} - \sigma^{iso}) + \cos2\alpha_{PR}(\sigma_{xx}^{PAS} - \sigma_{yy}^{PAS})]}\right] \end{aligned} \tag{14}$$

$$\begin{aligned} \delta_2 &= \tfrac{1}{2}\tan^{-1}\left(\frac{\sigma_{SIN2}}{\sigma_{COS2}}\right) \\ &= \tfrac{1}{2}\tan^{-1}\left[\frac{\cos\beta_{PR}\sin2\alpha_{PR}(\sigma_{xx}^{PAS} - \sigma_{yy}^{PAS})}{\tfrac{3}{2}\sin^2\beta_{PR}(\sigma_{zz}^{PAS} - \sigma^{iso}) + \tfrac{1}{2}(1 + \cos2\beta_{PR}) \times \cos2\alpha_{PR}(\sigma_{xx}^{PAS} - \sigma_{yy}^{PAS})}\right] \end{aligned} \tag{15}$$

Where the Euler angles (α_{PR}, β_{PR}, γ_{PR}) define the rotational transformation from the pincipal axis system (PAS) to the rotor fixed frame (RFF), and the principal element $\sigma_{ii}^{\ PAS}$ ($i = x, y, z$) denotes the element of the chemical shift tensor in the PAS. σ_{COSi} and σ_{SINi} (i = 1 and 2) are the projected elements of the i^{th}-order CSA Hamiltonian (σ_i) in x′y′ plane of the RFF, δ_i denotes the projection angle of CSA Hamiltonian σ_i relative to the x′ axis of the RFF.

Experimental section

Materials

The ^{15}N labeled *N*-acetyl-valine (NAV) and ^{13}C,^{15}N-labeled *N*-formyl-Met-Leu-Phe (MLF) tripeptide were purchased from Cambridge Isotope Laboratories. Both powder samples were packed into the MAS rotors for subsequent NMR experiments without any further purification or recrystallization.

NMR Experiments

All NMR experiments were carried out on a TECMAG Discovery spectrometer operating at a resonance frequency of 400.49 MHz for ^{1}H, 100.64 MHz for ^{13}C, and 40.55 MHz for ^{15}N. A 3.2 mm Varian triple-resonance probehead was used. The 3D pulse sequence that was used for correlating the dipolar and CSA tensors is displayed in Figure 2. All spectra were recorded at room temperature with a MAS frequency of 10 kHz. The typical 90° pulse lengths were 3.3 μs for ^{1}H and 4.8 μs for ^{15}N. The cross-polarization contact time was 1.0 ms, and the recycle delay was 3.0 s. Continuous wave (CW) ^{1}H decoupling with an rf field strength of 76 kHz was performed during the acquisition period and the residual part of the rotational echo period. During the $R14_2^{3/5}$ recoupling period, ^{1}H TPPM decoupling with an rf field strength of 76 kHz and ^{13}C XiX decoupling with an rf field strength of 69 kHz were carried out simultaneously. RF field strengths were 90 and 35 kHz for the $R18_1^{7}$ and $R14_2^{3/5}$ irradiation periods, respectively. The indirect dimensions (t_1 and t_2) of the 3D MAS experiments were incremented rotor-synchronously, by 100 μs and 200 μs, respectively. A total of 16 t_1 and 32 t_2 increments were used to record the 3D spectra, and 32 and 64 scans were accumulated for each increment, for *N*-acetyl-valine and *N*-formyl-Met-Leu-Phe, respectively. The data were processed by zero-filling and Fourier transformation in NMRPipe in a Mac environment. Zero-filling up to 256 points was performed in t_1 and t_2 dimensions, and line broadening of 100 Hz was applied in ω_1 and ω_2 during the processing.

Simulations of the NMR spectra

Numerical simulations of 1D and 2D NMR spectra were performed using the SIMPSON software package.[71] 986 ZCW angles (α, β) and 3 γ angles were used to generate a powder average. The ^{1}H Larmor frequency was set as 400.5 MHz, and a MAS frequency of 10 kHz was used for all simulations. The applied RF field intensities were 90 and 35 kHz for $R18_1^{7}$ and $R14_2^{3/5}$ irradiation, respectively. NMR parameters that are required as an input for the program are H-N dipolar couplings and the components of the ^{1}H and ^{15}N chemical shift anisotropy tensor, δ_σ and η. ^{1}H CSA with $\delta_\sigma = 8.9$ ppm and $\eta = 0.75$ was used for all simulations. Since the C-N heteronuclear dipolar couplings are completely averaged out by the XiX decoupling, carbon spins were not considered in any of the simulations. In order to determine the accurate relative orientation between the tensors, identical acquisition and processing parameters were used as in the simulations and the NMR experiments.

For defining the chemical shift tensor we follow the Haeberlen-Mehring-Spiess convention, where the isotropic value δ_{iso}, the reduced anisotropy δ_σ, the anisotropy Ω, and the asymmetry parameter η, are related to the principal elements of the chemical shift tensor according to $|\delta_{zz} - \delta_{iso}| \geq |\delta_{xx} - \delta_{iso}| \geq |\delta_{yy} - \delta_{iso}|$, $\delta_{iso} = ⅓(\delta_{xx} + \delta_{yy} + \delta_{zz})$, $\delta_{\sigma} = \delta_{zz} - \delta_{iso} = ⅔\Omega$., and $\eta = (\delta_{yy} - \delta_{xx})/(\delta_{zz} - \delta_{iso})$.

Density Functional Theory Calculations

^{15}N magnetic shielding anisotropy tensor calculations were performed in Gaussian03[72] using the B3LYP functional[73] and tzvp basis set.[74] The atomic coordinates were taken from the solid-state NMR structure of MLF[75] and used in the single-point calculations of the magnetic shielding anisotropy tensors without further geometry optimization. The calculated principal components of the magnetic shielding tensor, σ_{ii} (i = 1, 2, or 3), were converted to the principal components of the chemical shift tensors, δ_{ii}, using the relationship $\delta_{ii} = \sigma_{iso}(\text{ref}) - \sigma_{ii}$, where $\sigma_{iso}(\text{ref})$ = 244.6 ppm is the absolute shielding for liquid ammonia at 25 °C.[76]

Results and Discussion

Simulated DIP/CSA Correlation Spectra

Figure 3 illustrates the orientation of the principal axes of the amide nitrogen CSA in the common molecular frame. Euler angles α_{NH} and β_{NH} determine the relative orientation between the ^{15}N CSA and the ^{1}H-^{15}N dipolar tensors; this orientation yields important structural and dynamic information (i.e., torsion angle ϕ and backbone internal motional timescales in proteins). The relative orientation can be determined by correlating the H-N dipolar coupling, along the first indirect dimension ω_1, and the chemical shift anisotropy of the amide nitrogen, along the second indirect dimension ω_2. The 3D pulse sequence shown in Figure 2 was used to record such a 2D correlation spectrum extracted along the ^{15}N isotropic chemical shift dimension. After the ^{1}H-^{15}N cross polarization, the ^{15}N magnetization evolves during the t_1 period under the $R18_1^7$ Hamiltonian applied in the ^{1}H channel; this Hamiltonian reintroduces the ^{1}H-^{15}N dipolar couplings and the ^{1}H CSA interactions while suppressing the ^{1}H-^{1}H homonuclear dipolar couplings. Subsequently, the dipolar-modulated ^{15}N magnetization is tilted into the longitudinal direction and is subjected to the rf pulse irradiation of the $R14_2^3$ or $R14_2^5$ symmetry.

As discussed above, the $R14_2^3$ sequence has the same space-spin selection pathways and the same scaling factors as $R18_1^7$, where the ^{1}H-^{15}N/^{13}C-^{15}N heteronuclear dipolar couplings and the ^{15}N anisotropic chemical shift interactions are reintroduced. In order to achieve pure ^{15}N CSA interactions during the $R14_2^3$ pulse train period, TPPM and XiX heteronuclear decoupling is applied to protons and carbons, respectively. Usually, for efficient ^{1}H or ^{13}C decoupling a decoupling rf field strength greater than twice the rf field strength of the $R14_2^{3/5}$ element ($3.5\times\omega_R$) is required. The $R14_2^5$ symmetry sequence also recouples the ^{15}N-^{15}N homonuclear dipolar couplings while reintroducing the heteronuclear dipole-dipole and CSA interactions. It should be noted, however, that any effects of the ^{15}N-^{15}N dipolar couplings are negligible, given their small sizes (tens of Hertz). Therefore, the dipolar-modulated ^{15}N magnetization nutates under σ_1 or σ_2 γ-encoded CSA Hamiltonian during t_2, and is detected during t_3 in the presence of ^{1}H proton CW decoupling. The resulting 3D spectrum correlates ^{1}H-^{15}N dipolar couplings with the ^{15}N CSA interactions in two dimensions, and, in the third dimension, the isotropic ^{15}N chemical shift. Therefore it is easy to extract a 2D spectrum that correlates the dipolar and the CSA interactions along the ^{15}N isotropic chemical shift.

We analyzed the R-symmetry-based DIP/CSA correlation spectra for determining the relative orientation of the two tensors, using the SIMPSON simulation package. The simulated 2D DIP/CSA correlation spectra are shown in Figure 4 and correspond to different combined R-symmetry sequences. For both simulations, $R18_1^7$ is used for recoupling the ^{1}H-^{15}N dipolar interactions, while $R14_2^5$ and $R14_2^3$ are employed for recoupling the ^{15}N σ_1 and σ_2 CSA interactions as depicted in Figure 4a and 4b, respectively. To simulate the spectra, we constructed a molecular model consisting of two coupled (^{1}H, ^{15}N) spins with the same internal interaction parameters. For each spin, ^{1}H-^{15}N dipolar coupling and ^{1}H (or ^{15}N) chemical shift anisotropy tensors were included in the simulation. For the spectra shown in Figure 4, the principal frame of the ^{15}N chemical shift tensor was coincident with that of the anisotropic ^{1}H-^{15}N dipole-dipole interaction, i.e., $\alpha_{NH} = 0°$ and $\beta_{NH} = 0°$. Due to the different orientational dependence in the σ_2-CSA recoupled $R14_2^3$ and σ_1-CSA recoupled $R14_2^5$, different correlation spectra result from these two recoupling sequences as demonstrated in Figure 4 (a) and (b), respectively, even though the same R18 sequence is used for the ^{1}H-^{15}N dipolar recoupling during t_1 dimension.

Since the splitting of the recoupled lineshapes by γ-encoded $R18_1^7$ and $R14_2^{3/5}$ sequences depends greatly on the crystallite orientation in the laboratory frame (while the non γ-encoded recoupling schemes do not exhibit such orientational dependence), the 2D DIP/CSA correlation spectrum is sensitive to the relative orientation between the two tensors both in the crystalline and in the powder samples (simulated data are shown in the supporting information).

Figure 5 displays the simulated 2D $R18_1^7/R14_2^3$ DIP/CSA correlation spectra as the function of the relative tensor orientations; the corresponding $R18_1^7/R14_2^5$ spectra are shown in the Supporting Inforamation. From the series of these simulated spectra, it is clear that the powder lineshapes representing the DIP/CSA correlation are extremely sensitive to the orientation of the most deshielded element δ_{zz} relative to the N-H bond, represented by the Euler angle β_{NH}. The Euler angle α_{NH} affects the 2D correlation spectrum as well, but its effect on the lineshape is much less pronounced (simulated data shown in the Supporting Information). In all simulations, the δ_{xx} principal value of the CS A tensor is considered to lie in the Cα-N-H peptide plane ($\alpha_{NH} = 0°$). With the increase of the Euler angle β_{NH}, the lineshape spreads over a larger frequency range. These simulated 2D correlation plots demonstrate that it should be possible to extract the relative orientation between the dipolar and CSA tensors from the corresponding experimental spectra.

Experimental DIP/CSA Correlation Spectra

The applications of $R18_1^7$ for determining heteronuclear dipolar couplings have been reported previously.[26, 32, 40] However, the measurement of σ_1 or σ_2 CSA by $R14_2^{3/5}$ has not yet been investigated. Figure 6 shows the simulated and the experimental ^{15}N σ_1 and σ_2 CSA spectra of NAV generated by $R14_2^{3/5}$ symmetry sequences using an RF field intensity of 35 kHz for R14 irradiation. It can be seen that the scaling factor for recoupling the σ_1 CSA by $R14_2^5$ is higher than that for recoupling the σ_2 CSA by $R14_2^3$, although the σ_1 and σ_2 CSA lineshapes are similar. The central peak in the experimental spectra is assigned to the effect of finite ^{15}N relaxation times. The simulations yield a best-fit reduced anisotropy δ_σ of 103 ppm with an asymmetry parameter η of 0.25, and the simulated lineshapes agree well with the experimental spectra. These CSA parameters are also consistent with values reported previously.[62, 77] Our results demonstrate that γ-encoded $R14_2^{3/5}$ experiments can be performed to successfully determine the ^{15}N CSA tensors, and that $R14_2^5$ yields good accuracy in systems with weak homonuclear dipolar interactions (vide supra).

The experimental ^{1}H-^{15}N DIP/^{15}N CSA 2D correlation spectra of NAV obtained with the combined $R18_1^7/R14_2^{3/5}$ symmetry sequences are shown in Figures 7 (a) and 8 (a), respectively. The 2D lineshapes were extracted from the 3D correlation experiment (vide supra) along the ^{15}N isotropic chemical shift in the ω_3 dimension. $R14_2^5$ and $R14_2^3$ were performed to reintroduce the ^{15}N σ_1- (Figure 7(a)) and σ_2- (Figure 8(a)) CSA powder patterns, respectively. Consistent with the simulations discussed above, the experimental correlation spectra are different due to the different dependence of the lineshapes in each recoupling sequence on the relative tensor orientations. There also exists a central peak in the 2D correlation spectra arising from the ^{15}N relaxation, and its contribution to the overall spectrum makes it difficult to extract the DIP/CSA cross peaks cleanly, as shown in Figure 8(a). In order to determine the relative orientation between the ^{15}N CSA and ^{1}H-^{15}N dipolar tensors, a series of simulations are performed with Euler angles (α and β) monotonously increasing by 5°. Figures 7(b) and 8(b) show the best-fit simulated DIP/CSA correlation spectra for the 3D $R18_1^7/R14_2^5$ and $R18_1^7/R14_2^3$ sequences, respectively. The parameters used in the simulations, ^{1}H-^{15}N dipolar coupling ($\omega_{D(H\text{-}N)}$ = 10.4 kHz) and the ^{15}N CSA (δ_σ = 103 ppm and η = 0.25) were extracted from the simulated 1D $R18_1^7$ dipolar and $R14_2^5$ CSA patterns shown in Figure 6. For the $R18_1^7/R14_2^5$ experiment, the best-fit relative orientation was obtained for $\beta_{NH}(\delta_{zz}) = 25°\pm5°$ and $\alpha_{NH}(\delta_{xx}) = 30°\pm5°$. The best-fit simulated pattern was chosen visually, and the final error is estimated to be in range of ±5°. These angles establish unambiguously the orientation of ^{15}N CSA tensor in the quasi-molecular frame. Similarly, the best-fit relative orientation ($\beta_{NH}(\delta_{zz}) = 25°\pm5°$ and $\alpha_{NH}(\delta_{xx}) = 20°\pm10°$) was obtained for the 3D $R18_1^7/R14_2^3$ experiment. The consistency of the relative tensor orientations extracted from the two independent experiments is encouraging and illustrates the accuracy of the current approach. Figure 7(c, d) and Figure 8(c, d) show the DIP/CSA correlation patterns for other relative orientations. The orientation of ^{15}N CSA tensor in the molecular frame determined by the present NMR method agrees well with the previous reports.[62, 77] As can be observed, the ridge patterns depend to a large degree on the orientation of δ_{zz} relative to the N-H bond, and it is clear that there is a unique orientation that is consistent with the NMR experiment. Here it should be noted that the librational and vibrational motions would give rise to reduced CSA and dipolar interactions,[78] and this is commonly exploited in the studies of dynamics by CSA and dipolar recoupling techniques. These motions also add to the uncertainty in the experiments for measuring the relative orientation between CSA and dipolar tensors. A motionally averaged relative orientation would result in this case, especially for the system with librational motions where the relative orientation varies continuously over time.

The present combined symmetry sequences can also be applicable for simultaneous determination of DIP-CSA relative tensor orientations for multiple sites of interest. Figure 9 shows the ^{15}N σ_1 and σ_2 CSA recoupled NMR powder patterns of ^{13}C,^{15}N-enriched MLF tripeptide generated by γ-encoded $R14_2^3$ and $R14_2^5$ symmetry sequences; these powder patterns were extracted along the ^{15}N isotropic chemical shifts of each residue. The ^{15}N CSA parameters for each site can be derived from the experimental spectra using SIMPSON simulations. In Table 1, the best-fit ^{15}N CSA experimental parameters for MLF generated by the $R14_2^{3/5}$ symmetry-based recoupling sequences are compared with those obtained from quantum chemical calculations using DFT. It can be seen that the experimental ^{15}N CSA parameters derived from the $R14_2^{3/5}$ symmetry sequences generally agree with DFT computations very well. We note that there are small differences between the ^{15}N σ_1 and σ_2 CSA parameters extracted from the two pulse sequences, which we attribute to the effect of the ^{15}N relaxation on the central peak, as discussed above.

Three-dimensional $R18_1^7/R14_2^{3/5}$ experiments were also carried out on the MLF tripeptide for measuring the ^{15}N CSA orientation for each residue, as shown in Figure 10 (a – f). As discussed above, $R18_1^7$ and $R14_2^3$ or $R14_2^5$ are used for correlating the ^{1}H-^{15}N dipolar coupling and the ^{15}N σ_2 or σ_1 CSA interactions, respectively. 2D DIP/CSA correlation spectra for each residue were extracted from these 3D data sets along the ^{15}N isotropic chemical shift dimension (ω_3). SIMPSON simulations were carried out to derive the relative ^{1}H-^{15}N dipolar and ^{15}N CSA tensor orientations using the best-fit calculated ^{1}H-^{15}N dipolar coupling and the ^{15}N CSA parameters for each site, as shown in Table 2. The simulated best-fit DIP/CSA correlation powder patterns for each residue are shown in Figure

10 (g – l). Table 2 also lists the parameters obtained experimentally and computed using DFT. The comparison of experimental and DFT-calculated ^{15}N CSA parameters shown in Table 1, reveals that these are in good agreement, giving us confidence in both the experimental and computational methodologies. Although the ^{15}N orientation information obtained by DFT using b3lyp/tzvp method is slightly different from that derived from the symmetry-based NMR measurement, the difference is within the experimental error (see Table 2). Our results demonstrate that the amide nitrogen of each residue in the MLF tripeptide has a similar CSA tensor orientation relative to the H-N-Cα plane. The most deshielded element of the amide ^{15}N CSA tensor, δ_{zz}, is close to, but non-coincident with the H-N bond.

The experiments discussed above are generally applicable to peptides and proteins. The time for the 3D experiments introduced in this work is similar to that required for any 3D experiments on uniformly enriched proteins, and therefore, the same sensitivity considerations apply. The protein samples have to be stable over extended periods of time (days and up to several weeks), and instrument stability (rf fields, temperature, MAS frequency) is highly important. With the rapid progress in hardware (probes), data collection and sample preparation protocols, such as fast-MAS technology,[79-81] non-uniform sampling,[82, 83] use of paramagnetically doped samples to reduce the ^{1}H spin-lattice relaxation times and corresponding recycle delays without affecting other NMR observables,[84] as well as proton detection[6, 85] dramatic sensitivity enhancements are observed in multidimensional protein spectroscopy. A combination of these approaches enables 3D spectra to be detected in several hours rather than several days as we have seen in our laboratory (data to be reported elsewhere), making it possible to study very large and/or dilute proteins and protein assemblies. The information about the relative orientations of the CSA and dipolar tensors derived from the measurements introduced in this work is expected to be invaluable for accurate measurement of torsion angles, which in turn represent an important constraint in tertiary structure determination of peptides and proteins in the solid state.[86, 87]

Conclusions

In summary, combined R-symmetry sequences can be used to measure the relative orientations between the ^{1}H-^{15}N dipolar and ^{15}N chemical shift anisotropy tensors. γ-encoded $R14_2^5$ and $R14_2^3$ symmetry sequences are used to reintroduce the first-order (σ_1) and the second-order (σ_2) CSA powder patterns, respectively. These sequences work best at moderate MAS frequencies, which is the regime most commonly used for structural and dynamics studies in uniformly and extensively isotopically enriched peptides, proteins and protein assemblies. Each of these symmetry-based recoupling blocks can be combined with the $R18_1^7$ dipolar recoupling sequence to construct 2D dipolar/CSA correlation patterns. The ridges of these correlation spectra are very sensitive to the relative orientation between the two tensors. Since the dipolar and CSA principal components can be readily determined by independent measurements, the analysis of the spectral DIP/CSA correlation patterns is straightforward, with Euler angles $\beta_{NH}(\delta_{zz})$ and $\alpha_{NH}(\delta_{xx})$ being the only variable parameters. The latter can be readily extracted from the numerical simulations of the spectra. Our results show that the $\beta_{NH}(\delta_{zz})$ angle has the highest sensitivity to correlation patterns. The central peaks due to the ^{15}N relaxation contribute to the 1D/2D spectral lineshapes; these relaxation effects are necessary to be taken into account in the spectral simulations. Work is in progress on incorporating the effect of relaxation into the spectral simulations and on designing experiments that would minimize its influence on the experimental lineshapes. By incorporating a ^{15}N isotropic chemical shift dimension into a 3D experiment, these sequences become applicable for simultaneous determination of multiple sites in peptides and proteins, and are expected to become a useful tool for measuring torsion angles, important constraints in protein structure determination in the solid state.

Supplementary Material

Refer to Web version on PubMed Central for supplementary material.

Acknowledgments

This work was supported by the National Institutes of Health (NIH Grants P50GM082251 from NIGMS, P20 RR-015588 and 5P20RR017716-07 from the NCRR) and is a contribution from the Pittsburgh Center for HIV Protein Interactions. We thank Olga Dmytrenko for help with the DFT calculations, and Lex Vega for multiple discussions.

References

1. McDermott A, Polenova T. Curr Opin Struct Biol. 2007; 17:617–622. [PubMed: 17964133]
2. Huang L, McDermott AE. Biochim Biophys Acta. 2008; 1777:1098–1108. [PubMed: 18267103]
3. Hong M. Structure. 2006; 14:1731–1740. [PubMed: 17161364]
4. Seidel K, Andronesi OC, Krebs J, Griesinger C, Young HS, Becker S, Baldus M. Biochemistry. 2008; 47:4369–4376. [PubMed: 18355039]
5. Ader C, Schneider R, Seidel K, Etzkorn M, Becker S, Baldus M. J Am Chem Soc. 2009; 131:170–176. [PubMed: 19063626]
6. Zhou DH, Shah G, Mullen C, Sandoz D, Rienstra CM. Angew Chem Int Ed Engl. 2009; 48:1253–1256. [PubMed: 19130513]
7. Nanga RP, Brender JR, Vivekanandan S, Popovych N, Ramamoorthy A. J Am Chem Soc. 2009; 131:17972–17979. [PubMed: 19995078]
8. Shi L, Lake EM, Ahmed MA, Brown LS, Ladizhansky V. Biochim Biophys Acta. 2009; 1788:2563–2574. [PubMed: 19799854]
9. Tycko R. Quart Rev Biophys. 2006; 39:1.
10. Wasmer C, Lange A, Van Melckebeke H, Siemer AB, Riek R, Meier BH. Science. 2008; 319:1523–1526. [PubMed: 18339938]
11. Jaroniec CP, MacPhee CE, Bajaj VS, McMahon MT, Dobson CM, Griffin RG. Proc Natl Acad Sci U S A. 2004; 101:711–716. [PubMed: 14715898]
12. Helmus JJ, Surewicz K, Nadaud PS, Surewicz WK, Jaroniec CP. Proc Natl Acad Sci U S A. 2008; 105:6284–6289. [PubMed: 18436646]
13. Shon KJ, Kim Y, Colnago LA, Opella SJ. Science. 1991; 252:1303–1305. [PubMed: 1925542]
14. Thiriot DS, Nevzorov AA, Zagyanskiy L, Wu CH, Opella SJ. J Mol Biol. 2004; 341:869–879. [PubMed: 15288792]
15. Han Y, Ahn J, Concel J, Byeon IJ, Gronenborn AM, Yang J, Polenova T. J Am Chem Soc. 2010; 132:1976–1987. [PubMed: 20092249]
16. Sun S, Siglin A, Williams JC, Polenova T. J Am Chem Soc. 2009; 131:10113–10126. [PubMed: 19580321]
17. Lorieau JL, McDermott AE. J Am Chem Soc. 2006; 128:11505–11512. [PubMed: 16939274]
18. Lorieau JL, Day LA, McDermott AE. Proc Natl Acad Sci U S A. 2008; 105:10366–10371. [PubMed: 18653759]
19. Mainz A, Jehle S, van Rossum BJ, Oschkinat H, Reif B. J Am Chem Soc. 2009; 131:15968–15969. [PubMed: 19839609]
20. Giraud N, Blackledge M, Goldman M, Bockmann A, Lesage A, Penin F, Emsley L. J Am Chem Soc. 2005; 127:18190–18201. [PubMed: 16366572]
21. Bockmann A, Juy M, Bettler E, Emsley L, Galinier A, Penin F, Lesage A. J Biomol NMR. 2005; 32:195–207. [PubMed: 16132820]

22. Lesage A, Emsley L, Penin F, Bockmann A. J Am Chem Soc. 2006; 128:8246–8255. [PubMed: 16787089]
23. Wylie BJ, Sperling LJ, Frericks HL, Shah GJ, Franks WT, Rienstra CM. J Am Chem Soc. 2007; 129:5318–5319. [PubMed: 17425317]
24. Wylie B, Schwieters CD, Oldfield E, Rienstra C. J Am Chem Soc. 2009; 131:985–992. [PubMed: 19123862]
25. Yang J, Tasayco ML, Polenova T. J Am Chem Soc. 2008; 130:5798–5807. [PubMed: 18393505]
26. Yang J, Tasayco ML, Polenova T. J Am Chem Soc. 2009; 131:13690–13702. [PubMed: 19736935]
27. Baldus M. Prog Nucl Magn Reson Spectrosc. 2002; 41:1–47.
28. Tycko R. Prog Nucl Magn Reson Spectrosc. 2003; 42:53–68.
29. Ernst, RR.; Bodenhausen, G.; Wokaun, A. Principles of nuclear magnetic resonance in one and two dimensions. Oxford University Press; New York: 1987.
30. Schmidt-Rohr, K.; Spiess, HW. Multidimensional solid-state NMR and polymers. Academic Press; London; San Diego: 1994.
31. Franks WT, Zhou DH, Wylie BJ, Money BG, Graesser DT, Frericks HL, Sahota G, Rienstra CM. J Am Chem Soc. 2005; 127:12291–12305. [PubMed: 16131207]
32. Franks WT, Wylie B, Schmidt HL, Nieuwkoop AJ, Mayrhofer RM, Shah GJ, Graesser DT, Rienstra C. Proc Natl Acad Sci U S A. 2008; 105:4621–4626. [PubMed: 18344321]
33. Hohwy M, Jaroniec CP, Reif B, Rienstra CM, Griffin RG. J Am Chem Soc. 2000; 122:3218–3219.
34. Kandasamy SK, Lee DK, Nanga RP, Xu J, Santos JS, Larson RG, Ramamoorthy A. Biochim Biophys Acta. 2009; 1788:686–695. [PubMed: 19071084]
35. Chan JCC, Tycko R. J Chem Phys. 2003; 118:8378–8389.
36. Duma L, Abergel D, Ferrage F, Pelupessy P, Tekely P, Bodenhausen G. Chem Phys Chem. 2008; 9:1104–1106. [PubMed: 18425737]
37. Mehta MA, Eddy MT, McNeill SA, Mills FD, Long JR. J Am Chem Soc. 2008; 130:2202–2212. [PubMed: 18220389]
38. Schnell I. Prog Nucl Magn Reson Spectrosc. 2004; 45:145–207.
39. Kehlet CT, Sivertsen AC, Bjerring M, Reiss TO, Khaneja N, Glaser SJ, Nielsen NC. J Am Chem Soc. 2004; 126:10202–10203. [PubMed: 15315406]
40. Zhao X, Eden M, Levitt MH. Chem Phys Lett. 2001; 342:353–361.
41. Verel R, Ernst M, Meier BH. J Magn Reson. 2001; 150:81–99. [PubMed: 11330986]
42. Bennett AE, Weliky DP, Tycko R. J Am Chem Soc. 1998; 120:4897–4898.
43. Fu R, Smith SA, Bodenhausen G. Chem Phys Lett. 1997; 272:361–369.
44. Ernst M, Bush S, Kolbert AC, Pines A. J Chem Phys. 1996; 105:3387–3397.
45. Wei YF, Lee DK, McDermott AE, Ramamoorthy A. J Magn Reson. 2002; 158:23–35. [PubMed: 12419668]
46. Lee DK, Wei YF, Ramamoorthy A. J Phys Chem B. 2001; 105:4752–4762.
47. Wei YF, Lee DK, Ramamoorthy A. Chem Phys Lett. 2000; 324:20–24.
48. Poon A, Birn J, Ramamoorthy A. J Phys Chem B. 2004; 108:16577–16585. [PubMed: 18449362]
49. Chen L, Wang Q, Hu BW, Lafon O, Trebosc J, Deng F, Amoureux JP. Phys Chem Chem Phys. 2010; 12:9395–9405. [PubMed: 20577687]
50. Lorigan GA, McNamara R, Jones RA, Opella SJ. J Magn Reson. 1999; 140:315–319. [PubMed: 10497038]
51. Nevzorov AA, Opella SJ. J Magn Reson. 2003; 160:33–39. [PubMed: 12565046]
52. Denny JK, Wang J, Cross TA, Quine JR. J Magn Reson. 2001; 152:217–226. [PubMed: 11567575]
53. Traaseth NJ, Shi L, Verardi R, Mullen DG, Barany G, Veglia G. Proc Natl Acad Sci U S A. 2009; 106:10165–10170. [PubMed: 19509339]
54. Lee DK, Wittebort RJ, Ramamoorthy A. J Am Chem Soc. 1998; 120:8868–8874.
55. van Rossum BJ, de Groot CP, Ladizhansky V, Vega S, de Groot HJM. J Am Chem Soc. 2000; 122:3465–3472.

56. Tycko R. J Chem Phys. 2007; 126:064506. [PubMed: 17313228]
57. Eden M. Chem Phys Lett. 2003; 378:55–64.
58. Brinkmann A, Levitt MH. J Chem Phys. 2001; 115:357–384.
59. Eden M, Levitt MH. J Chem Phys. 1999; 111:1511–1519.
60. Carravetta M, Eden M, Zhao X, Brinkmann A, Levitt MH. Chem Phys Lett. 2000; 321:205–215.
61. DeDios AC, Pearson JG, Oldfield E. Science. 1993; 260:1491–1496. [PubMed: 8502992]
62. Brender JR, Taylor DM, Ramamoorthy A. J Am Chem Soc. 2001; 123:914–922. [PubMed: 11456625]
63. Jurd APS, Titman JJ. Phys Chem Chem Phys. 2009; 11:6999–7007. [PubMed: 19652834]
64. Andronesi OC, Pfeifer JR, Al-Momani L, Ozdirekcan S, Rijkers DT, Angerstein B, Luca S, Koert U, Killian JA, Baldus M. J Biomol NMR. 2004; 30:253–265. [PubMed: 15754053]
65. Ishii Y, Terao T, Kainosho M. Chem Phys Lett. 1996; 256:133–140.
66. Ramamoorthy A, Opella SJ. Solid State Nucl Magn Reson. 1995; 4:387–392. [PubMed: 8581437]
67. Schmidt-Rohr K. J Am Chem Soc. 1996; 118:7601–7603.
68. Yao XL, Hong M. J Am Chem Soc. 2002; 124:2730–2738. [PubMed: 11890824]
69. Nishiyama Y, Yamazaki T, Terao T. J Chem Phys. 2006; 124:064304.
70. Lee YK, Kurur ND, Helmle M, Johannessen OG, Nielsen NC, Levitt MH. Chem Phys Lett. 1995; 242:304–309.
71. Bak M. J Magn Reson. 2000; 147:296–330. [PubMed: 11097821]
72. Frisch, MJ.; Trucks, GW.; Schlegel, HB.; Scuseria, GE.; Robb, MA.; Cheeseman, JR.; Montgomery, JA.; Vreven, T.; Kudin, KN.; Burant, JC.; Millam, JM.; Iyengar, SS.; Tomasi, J.; Barone, V.; Mennucci, B.; Cossi, M.; Scalmani, G.; Rega, N.; Petersson, GA.; Nakatsuji, H.; Hada, M.; Ehara, M.; Toyota, K.; Fukuda, R.; Hasegawa, J.; Ishida, M.; Nakajima, T.; Honda, Y.; Kitao, O.; Nakai, H.; Klene, M.; Li, X.; Knox, JE.; Hratchian, HP.; Cross, JB.; Bakken, V.; Adamo, C.; Jaramillo, J.; Gomperts, R.; Stratmann, RE.; Yazyev, O.; Austin, AJ.; Cammi, R.; Pomelli, C.; Ochterski, JW.; Ayala, PY.; Morokuma, K.; Voth, GA.; Salvador, P.; Dannenberg, JJ.; Zakrzewski, VG.; Dapprich, S.; Daniels, AD.; Strain, MC.; Farkas, O.; Malick, DK.; Rabuck, AD.; Raghavachari, K.; Foresman, JB.; Ortiz, JV.; Cui, Q.; Baboul, AG.; Clifford, S.; Cioslowski, J.; Stefanov, BB.; Liu, G.; Liashenko, A.; Piskorz, P.; Komaromi, I.; Martin, RL.; Fox, DJ.; Keith, T.; Laham, A.; Peng, CY.; Nanayakkara, A.; Challacombe, M.; Gill, PMW.; Johnson, B.; Chen, W.; Wong, MW.; Gonzalez, C.; Pople, JA. Gaussian 03, revision C.02. Gaussian, Inc.; Wallingford, CT: 2004.
73. Becke AD. J Chem Phys. 1993; 98:5648–5652.
74. Schafer A, Horn H, Ahlrichs R. J Chem Phys. 1992; 97:2571–2577.
75. Rienstra CM, Tucker-Kellogg L, Jaroniec CP, Hohwy M, Reif B, McMahon MT, Tidor B, Lozano-Perez T, Griffin RG. Proc Natl Acad Sci U S A. 2002; 99:10260–10265. [PubMed: 12149447]
76. Jameson CJ, Jameson AK, Cohen SM, Parker H, Oppusunggu D, Burrell PM, Wille S. J Chem Phys. 1981; 74:1608–1612.
77. Facelli JC, Pugmire RJ, Grant DM. J Am Chem Soc. 1996; 118:5488–5489.
78. Hallock KJ, Lee DK, Ramamoorthy A. J Chem Phys. 2000; 113:11187–11193.
79. Samoson A, Tuherm T, Gan Z. Solid State Nucl Magn Reson. 2001; 20:130–136. [PubMed: 11846236]
80. Ernst M, Meier MA, Tuherm T, Samoson A, Meier BH. J Am Chem Soc. 2004; 126:4764–4765. [PubMed: 15080665]
81. Samoson A, Tuherm T, Past J, Reinhold A, Anupold T, Heinmaa N. New Techniques in Solid-State NMR. 2005; 246:15–31.
82. Rovnyak D, Frueh DP, Sastry M, Sun ZYJ, Stern AS, Hoch JC, Wagner G. J Magn Reson. 2004; 170:15–21. [PubMed: 15324754]
83. Petkova AT, Baldus M, Belenky M, Hong M, Griffin RG, Herzfeld J. J Magn Reson. 2003; 160:1–12. [PubMed: 12565042]
84. Wickramasinghe NP, Shaibat M, Ishii Y. J Am Chem Soc. 2005; 127:5796–5797. [PubMed: 15839671]

85. Zhou DH, Shah G, Cormos M, Mullen C, Sandoz D, Rienstra CM. J Am Chem Soc. 2007; 129:11791–11801. [PubMed: 17725352]
86. Rienstra CM, Hohwy M, Mueller LJ, Jaroniec CP, Reif B, Griffin RG. J Am Chem Soc. 2002; 124:11908–11922. [PubMed: 12358535]
87. Chan JCC, Tycko R. J Am Chem Soc. 2003; 125:11828–11829. [PubMed: 14505399]

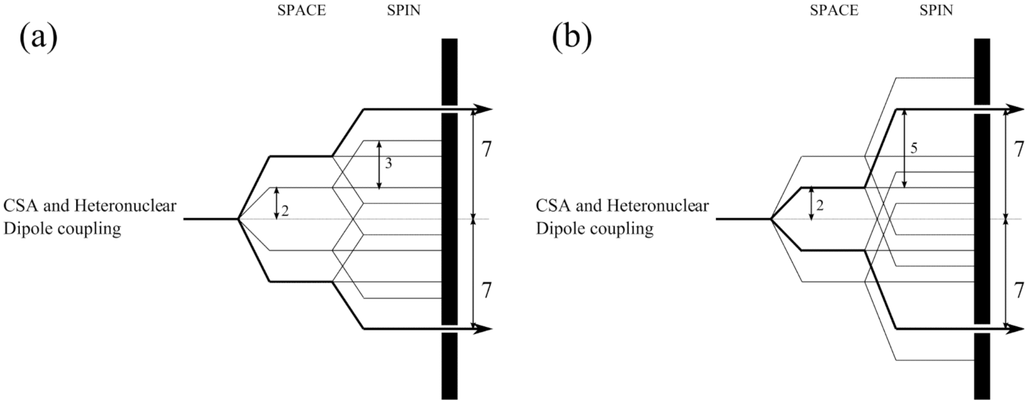

Figure 1.

Space-spin selection diagrams for $R14_2^3$ (a) and $R14_2^5$ (b). (a) $R14_2^3$ selects the components of the heteronuclear dipolar and CSA interactions with quantum numbers $\{l, m, \lambda, \mu\} = \{2, 2, 1, -1\}$ and $\{2, -2, 1, 1\}$, respectively. (b) $R14_2^5$ selects the components of the heteronuclear dipolar and CSA interactions with quantum numbers $\{l, m, \lambda, \mu\} = \{2, 1, 1, -1\}$ and $\{2, -1, 1, 1\}$, respectively.

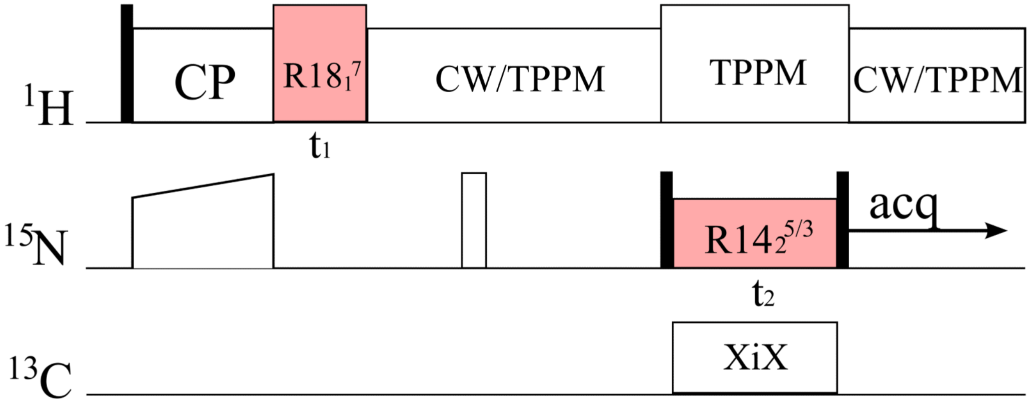

Figure 2.

Pulse sequence for the three-dimensional CSA/DIP orientational correlation experiment. Solid and blank squares denote $\pi/2$ and π pulses, respectively. ^{1}H-^{15}N dipolar coupling and ^{15}N CSA interactions are reintroduced by the γ-encoded symmetry sequences $R18_1^7$ and $R14_2^{5/3}$ in the indirect t_1 and t_2 dimensions, respectively.

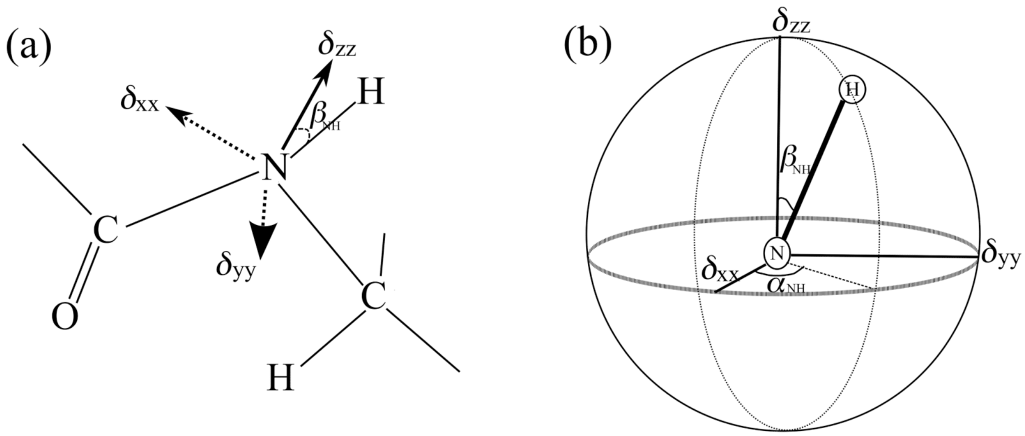

Figure 3.

(a) Molecular structure of a peptide unit depicting the orientation of chemical shift tensor of the amide nitrogen in the molecular frame, defined by the N-H bond (*z*-axis) and the C-N-H peptide plane. (b) Euler rotations between the principal axis system (PAS) of the CSA tensor and the molecular frame. Euler angles α_{NH} and β_{NH} represent the orientation of the three principal elements of ^{15}N CSA tensor in the peptide unit. The peptide plane contains the N-H bond and the δ_{zz} principal component of the ^{15}N CSA tensor as shown in (b), with a zero Euler angle γ.

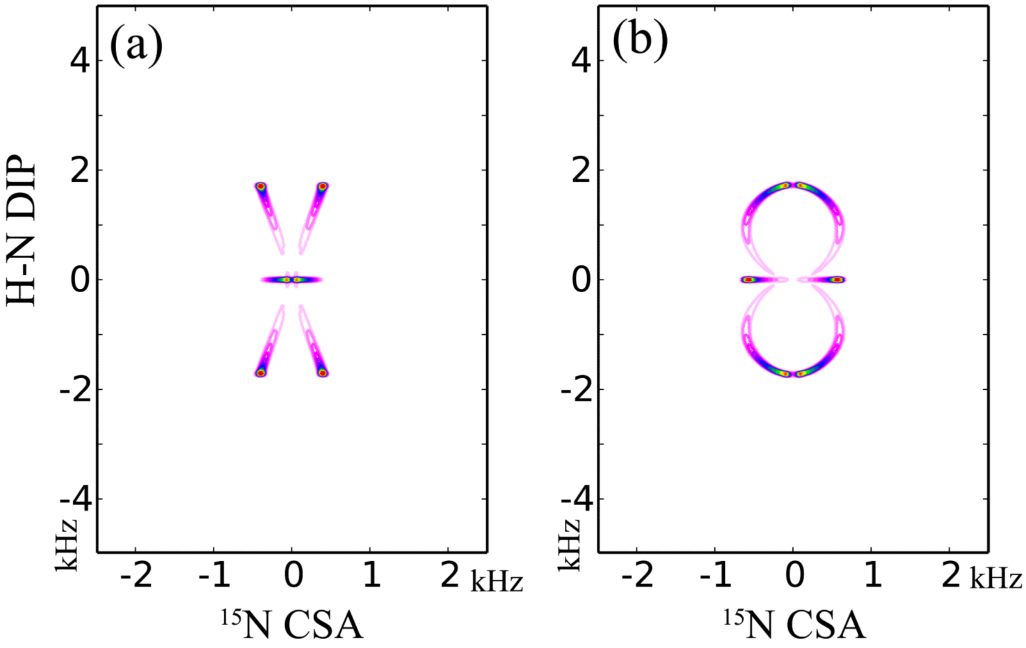

Figure 4.

Simulated CSA/DIP correlation NMR spectra produced by combined symmetry-based sequences, $R18_1^7/R14_2^3$ (a) and $R18_1^7/R14_2^5$ (b). The CSA and dipolar tensors are assumed to be coincident in this simulation (α_{NH} = 0° and β_{NH} = 0°). 64 t_1 increments and 128 t_2 increments were used to generate the spectra.

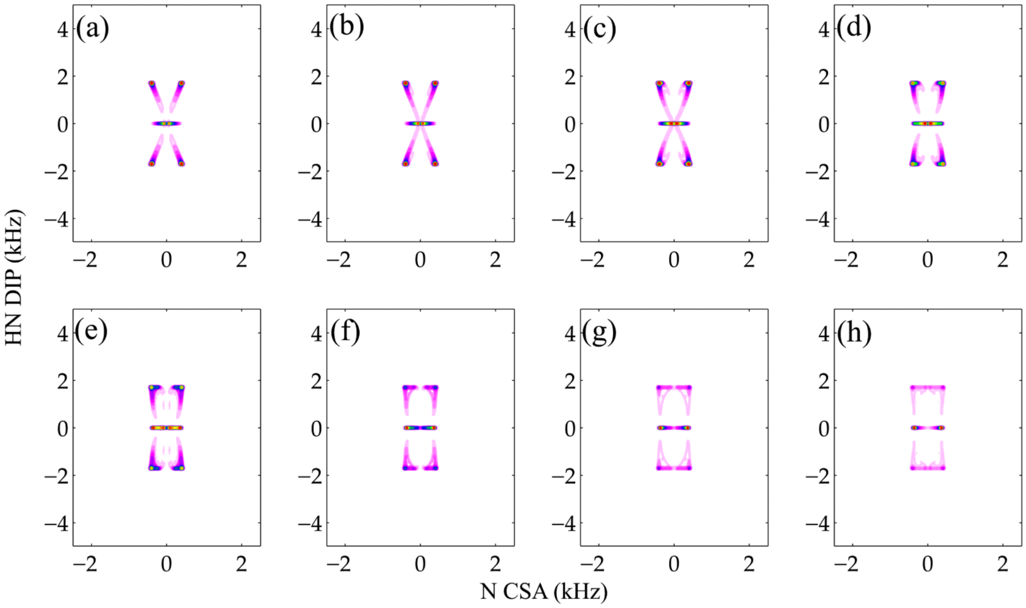

Figure 5.

Simulated R18_1^7/R14_2^3 CSA/DIP spectra for different relative tensor orientations. In these simulations, the δ_{xx} principal value CSA is considered to lie in the Cα-N-H peptide plane ($\alpha_{NH} = 0°$), and the angle β_{NH} between the H-N vector and the CSA δ_{zz} principal value was changed from 0 to 70 degrees with 10-degree increments from (a) to (h), respectively. 64 t_1 increments and 128 t_2 increments were used for each simulation. A powder average was generated with 986 ZCW angles and 3 γ angles.

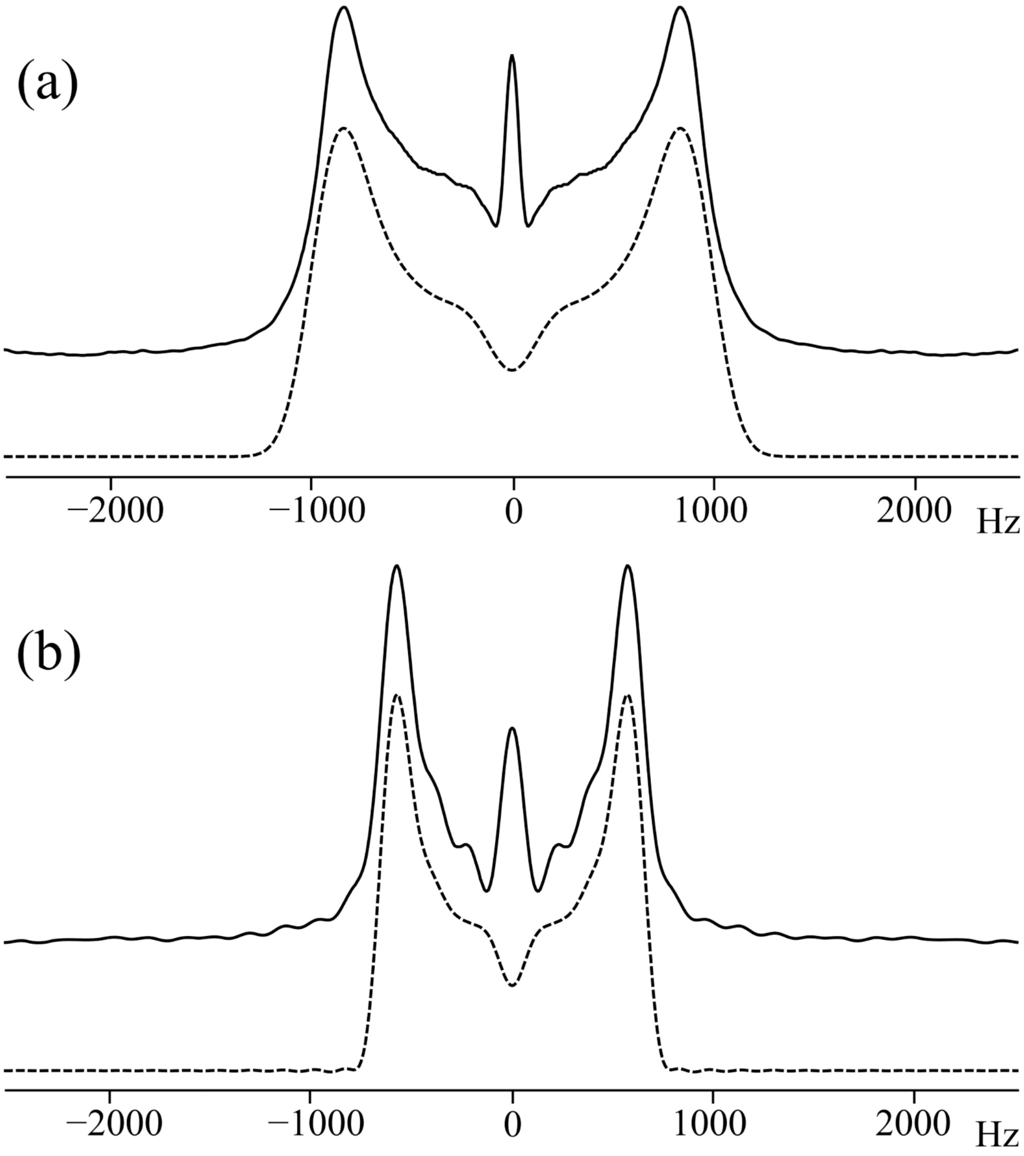

Figure 6.

Experimental (solid lines) and simulated (dashed lines) σ_1 and σ_2 CSA recoupled ^{15}N NMR spectra of [^{15}N]-N-acetyl-valine (NAV) generated by γ-encoded R14_2^5 (a) and R14_2^3(b) sequences, respectively. The sample was spun at an MAS frequency of 10 kHz. In both 2D experiments, 32 scans were accumulated for each t_1 increment. A total of 32 t_1 increments were used. The acquisition and processing parameters used in SIMPSON simulations were the same as those utilized in the corresponding NMR experiments. The best-fit simulated spectra were obtained with δ_σ = 103 ppm and η = 0.25.

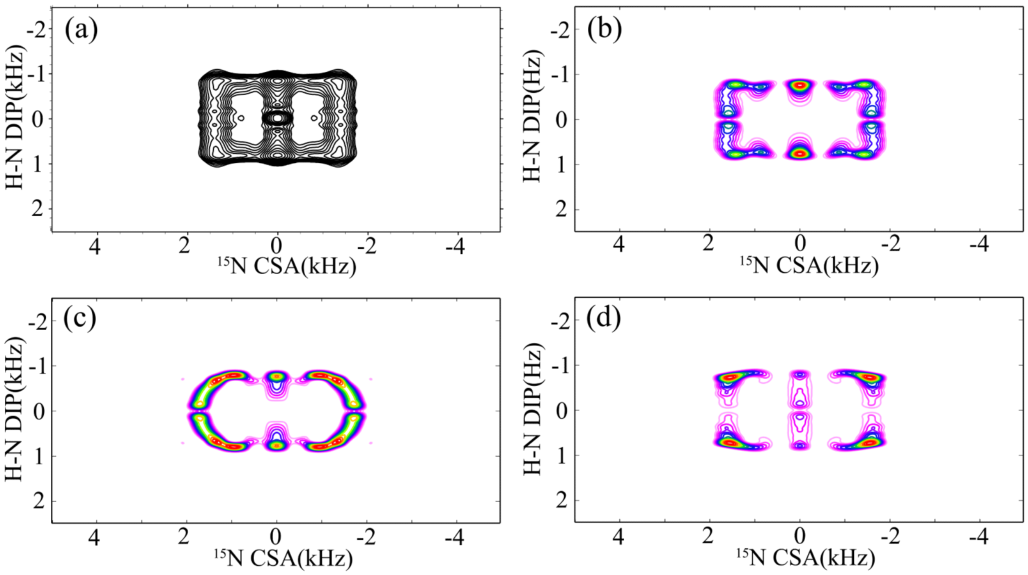

Figure 7.

(a) 2D ^{15}N CSA/^{1}H-^{15}N DIP correlation spectrum of *N*-acetyl-valine (NAV), extracted from the 3D $R18_1^7/R14_2^5$ experiment along the ^{15}N isotropic chemical shift. The spectrum was recorded with 64 scans, 16 t_1 and 32 t_2 increments. The sample was spun at a MAS frequency of 10 kHz. (b) Best-fit simulated correlation spectrum, obtained with $\beta_{\mathrm{NH}}(\delta_{\mathrm{zz}})$ = 25°±5° and $\alpha_{NH}(\delta_{\mathrm{xx}})$ = 30°±10°, using the same acquisition and processing parameters as in the NMR experiment in (a). (c) Simulated correlation spectrum with $\beta_{\mathrm{NH}}(\delta_{\mathrm{zz}})$ = 0° and α_{NH} (δ_{xx}) = 0°. (d) Simulated correlation spectrum with $\beta_{\mathrm{NH}}(\delta_{\mathrm{zz}})$ = 90° and $\alpha_{NH}(\delta_{\mathrm{xx}})$ = 0°.

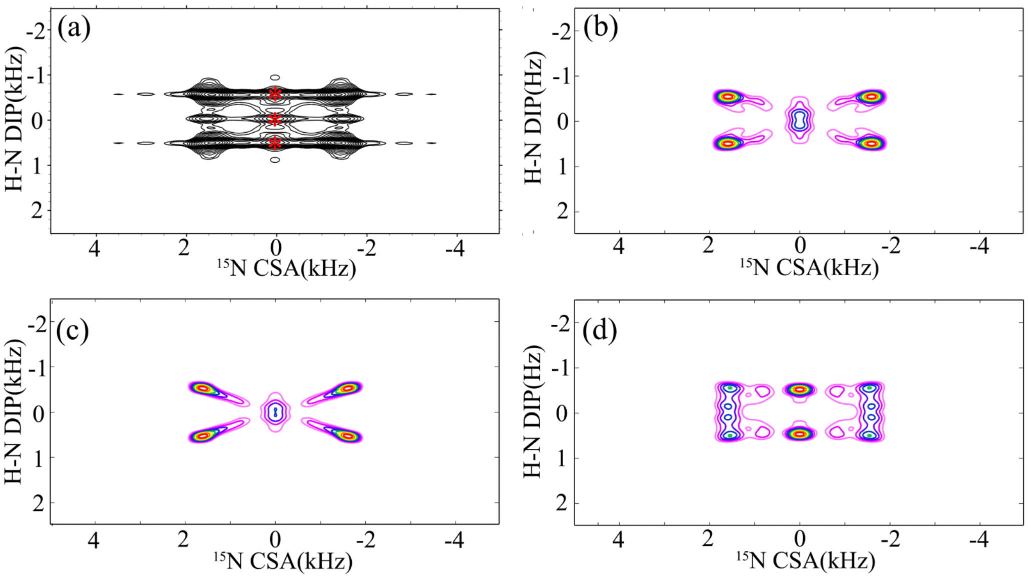

Figure 8.

(a) 2D ^{15}N CSA/^{1}H-^{15}N DIP correlation spectrum of *N*-acetyl-valine (NAV), extracted from the 3D R18_1^7/R14_2^3 experiment along the ^{15}N isotropic chemical shift. The spectrum was recorded with 64 scans, 16 t_1 and 32 t_2 increments. The sample was spun at a MAS frequency of 10 kHz. (b) Best-fit simulated correlation spectrum, obtained with $\beta_{NH}(\delta_{zz})$ = 25°±5° and $\alpha_{NH}(\delta_{xx})$ = 20°±5°, and the same acquisition and processing parameters as in the NMR experiment. (c) Simulated correlation spectrum with $\beta_{NH}(\delta_{zz}) = 0°$ and $\alpha_{NH}(\delta_{xx}) = 0°$. (d) Simulated correlation spectrum with $\beta_{NH}(\delta_{zz}) = 90°$ and $\alpha_{NH}(\delta_{xx}) = 0°$.

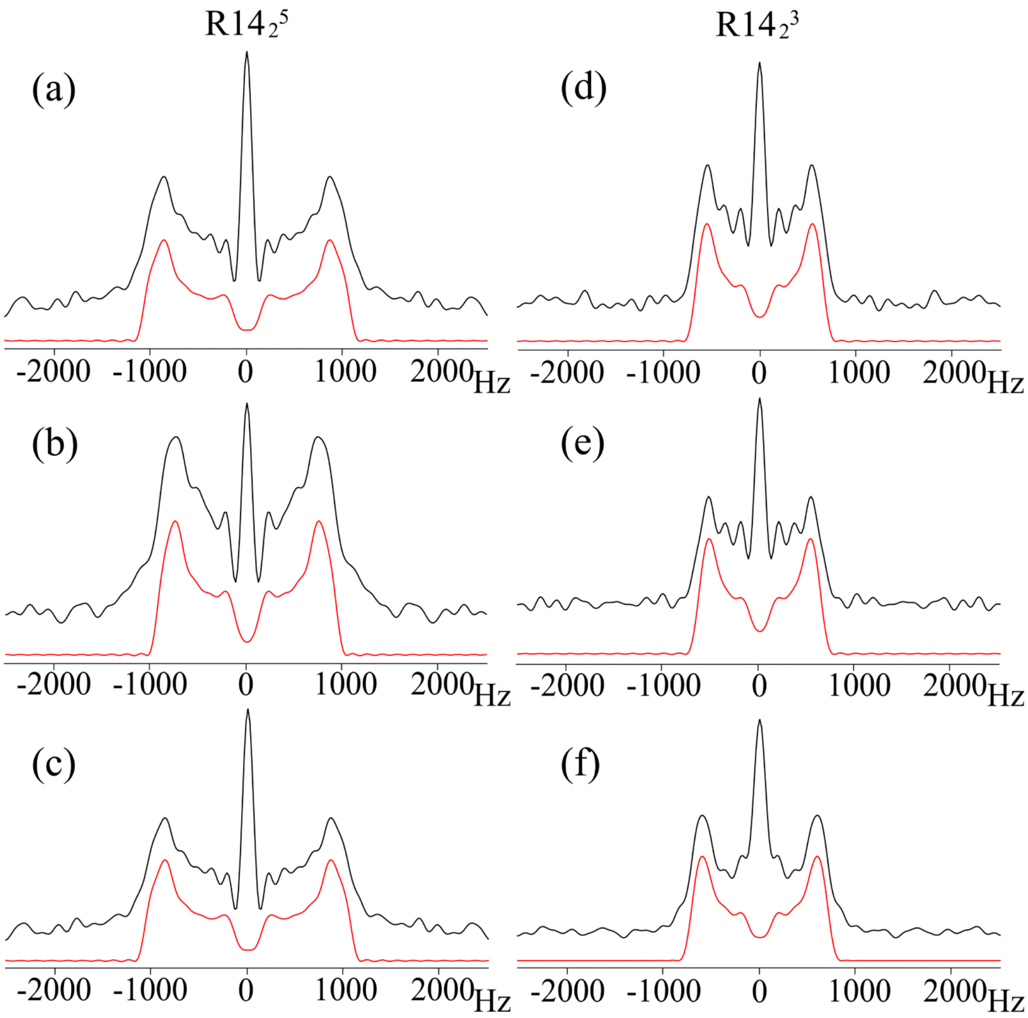

Figure 9.

^{15}N σ_1 and σ_2 CSA recoupled NMR spectra of ^{13}C, ^{15}N *N*-formyl-Met-Leu-Phe (MLF) tripeptide, for Phe (a, d), Leu (b, e), and Met (c, f) residues. The spectra were recorded using R14$_2^5$ (a - c) and R14$_2^3$ (d - e) pulse sequences, respectively. The sample was spun at a MAS frequency of 10 kHz. The experimental spectra are shown in black, the best-fit spectra simulated in SIMPSON, in red. The best-fit chemical shift anisotropy δ_σ and asymmetry parameter η as well as the comparison with other experimental and computational results are presented in Table 1.

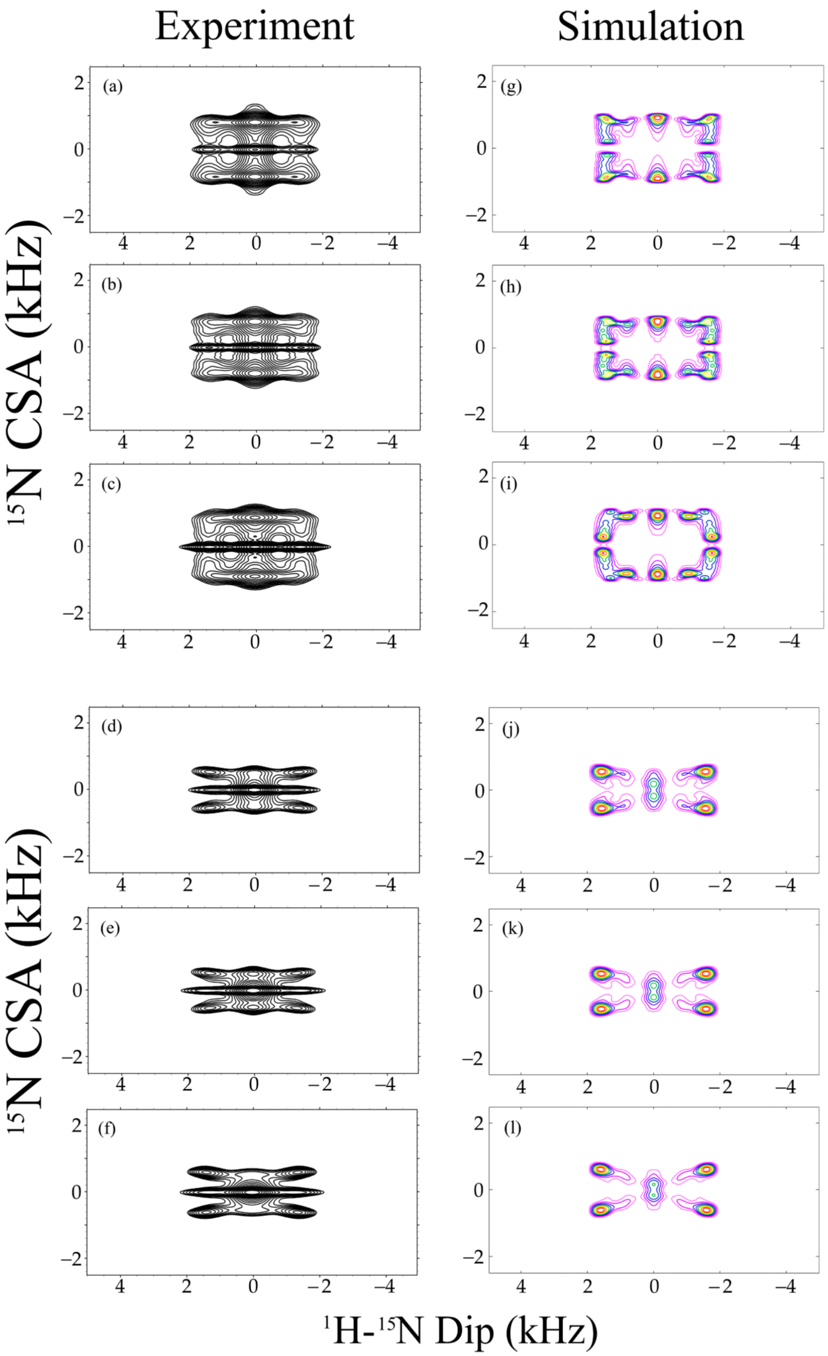

Figure 10.

Experimental (a-f) and simulated (g-l) ^{15}N CSA/^{1}H-^{15}N dipolar correlation spectra of ^{13}C, ^{15}N *N*-formyl-Met-Leu-Phe (MLF) tripeptide, extracted from the corresponding 3D experiments along the ^{15}N isotropic chemical shift for Phe (a, d), Leu (b, e) and Met (c, f) residues. 3D $R18_1^7/R14_2^5$ and $R18_1^7/R14_2^3$ pulse sequences were used to record the experimental (a - c) and (d - f) spectra, respectively, and the same sequences were employed to generate the simulated (g – i) and (j – l) spectra, respectively. The sample was spun at a MAS frequency of 10 kHz. ^{1}H-^{15}N dipolar and ^{15}N CSA parameters used in the simulations were extracted from 1D R18 dipolar and 1D R14 CSA pattern simulations, and fixed during the calculations. The orientation of the ^{15}N CSA relative to ^{1}H-^{15}N dipolar tensor was optimized. The best-fit relative orientations between the ^{1}H-^{15}N dipolar and ^{15}N CSA are shown in Table 2.

Table 1

^{15}N CSA parameters for each residue in ^{13}C, ^{15}N *N*-formyl-MLF: experimental derived from $R14_2^{3/5}$ recoupling sequences and calculated using Density Functional Theory. The experimental and simulated σ_1 and σ_2 CSA powder patterns are shown in Figure 9.

Residue	**Method**	**δ_{iso}(ppm)**	**δ_{σ}ppm)**	**η_{σ}**
Met	$R14_2^5$	125.5	107±1	0.33±0.01
	$R14_2^3$	125.5	109±1	0.32±0.01
	DFT: b3lyp/tzvp	117.3	110.4	0.40
Leu	$R14_2^5$	116.2	93±1	0.34±0.01
	$R14_2^3$	116.2	97±1	0.35±0.01
	DFT: b3lyp/tzvp	112.6	93.2	0.70
Phe	$R14_2^5$	107.6	101±1	0.32±0.01
	$R14_2^3$	107.6	101±1	0.34±0.01
	DFT: b3lyp/tzvp	103.7	97.0	0.40

Table 2

The relative orientations between ^{1}H-^{15}N dipolar and ^{15}N CSA tensors for each residue in ^{13}C, ^{15}N *N*-formyl-MLF: experimental derived from $R18_1^7/R14_2^{3/5}$ recoupling sequences and calculated using Density Functional Theory.

Residue	**Method**	**α_{NH} (degrees)**	**β_{NH} (degrees)**
Met	$R18_1^7/R14_2^{3/5}$	20±10	20±5
	DFT: b3lyp/tzvp	9.8	14.8
Leu	$R18_1^7/R14_2^{3/5}$	20±10	25±5
	DFT: b3lyp/tzvp	6.3	14.7
Phe	$R18_1^7/R14_2^{3/5}$	10±10	35±10
	DFT: b3lyp/tzvp	24	19